Journal of Biomedical Optics

BiomedicalOptics.SPIEDigitalLibrary.org

Performance of computer vision *in vivo* flow cytometry with low fluorescence contrast

Stacey Markovic
Siyuan Li
Mark Niedre

SPIE.

Performance of computer vision *in vivo* flow cytometry with low fluorescence contrast

Stacey Markovic,* Siyuan Li, and Mark Niedre
Northeastern University, Department of Electrical and Computer Engineering, 360 Huntington Avenue, Boston, Massachusetts 02115, United States

Abstract. Detection and enumeration of circulating cells in the bloodstream of small animals are important in many areas of preclinical biomedical research, including cancer metastasis, immunology, and reproductive medicine. Optical *in vivo* flow cytometry (IVFC) represents a class of technologies that allow noninvasive and continuous enumeration of circulating cells without drawing blood samples. We recently developed a technique termed computer vision *in vivo* flow cytometry (CV-IVFC) that uses a high-sensitivity fluorescence camera and an automated computer vision algorithm to interrogate relatively large circulating blood volumes in the ear of a mouse. We detected circulating cells at concentrations as low as 20 cells/mL. In the present work, we characterized the performance of CV-IVFC with low-contrast imaging conditions with (1) weak cell fluorescent labeling using cell-simulating fluorescent microspheres with varying brightness and (2) high background tissue autofluorescence by varying autofluorescence properties of optical phantoms. Our analysis indicates that CV-IVFC can robustly track and enumerate circulating cells with at least 50% sensitivity even in conditions with two orders of magnitude degraded contrast than our previous *in vivo* work. These results support the significant potential utility of CV-IVFC in a wide range of *in vivo* biological models. [DOI: 10.1117/1.JBO.20.3.035005]

Keywords: *in vivo* flow cytometry; computer vision; low contrast; rare circulating cells.

Paper 140777R received Nov. 24, 2014; accepted for publication Mar. 3, 2015; published online Mar. 30, 2015.

1 Introduction

There are many areas of biomedical research where detection and enumeration of rare circulating cells in the bloodstream of small animals are important, including cancer metastasis, hematological malignancies, immunology, and reproductive medicine.[1–7] The classical method for enumerating circulating cells is to draw small peripheral blood (PB) samples from the animals, which are subsequently analyzed with techniques such as flow cytometry, fluorescence microscopy, or more recently with microfluidic devices.[8–12] However, this "*ex-vivo*" approach is known to be fundamentally problematic, since handling, storage, and enrichment of PB samples have been shown to affect cell viability and behavior.[13–16] These limitations motivated the development of "*in vivo* flow cytometry" (IVFC) technology by Lin et al. in 2004,[17,18] wherein circulating cells are optically counted without the need for drawing blood samples. Briefly, in IVFC, a laser slit illuminates a small blood vessel in the ear or retina of a mouse. As fluorescently labeled cells pass through the field of view (FOV), fluorescent "spikes" are detected by the instrument. As such, circulating cells can be noninvasively and continuously counted *in vivo* allowing, for example, detection of rapid changes in circulating cell populations over time in response to drug treatment.[19–21] Other IVFC variants have also been developed, including multiphoton IVFC, photo-acoustic flow cytometry, and photo-thermal flow cytometry.[22–30] IVFC has been used for the *in vivo* study of many cell types, including breast cancer, prostate cancer, hepatocellular carcinoma cells, melanoma, multiple myeloma, T-lymphocytes, infections, and sickle cells.[18,21,22,28–36]

Despite its great utility in small animal research, IVFC has one significant limitation: the relatively low cell detection sensitivity, which is a consequence of the small blood vessels that are sampled. Specifically, blood flow rates in an ear arteriole are on the order of 1 μL/min, whereas a mouse has approximately 2 mL of circulating blood. Therefore, in a 15-min scan, only about 1% of the total circulating blood volume is sampled, so that low-abundance cell types may be entirely missed. Motivated by this limitation, our group (and others[31,32]) has developed new IVFC approaches that interrogate larger circulating blood volumes and, therefore, increase detection sensitivity.[37–41]

Most relevant to the present work, we recently developed and validated a technique termed Computer Vision IVFC (CV-IVFC).[40] Briefly, we developed an instrument that utilizes macroscopic fluorescence imaging of a relatively large (5×5 mm^2) region of a mouse ear, where circulating blood volumes are on the order of 10–15 μL/min, i.e., an order of magnitude greater than microscopy-IVFC. The imager used a red (660 nm) excitation laser and a filtered high-sensitivity electron multiplied charge-coupled device (EMCCD) camera that acquired fluorescence images with a 19 Hz frame rate. As fluorescently labeled circulating cells passed through the ear, they were detected by the camera. We also developed an algorithm to automatically detect and track circulating cells from the image sequences. This was necessary for three reasons: (1) the rarity of the low-abundance cells that we

*Address all correspondence to: Stacey Markovic, E-mail: markovic.s@husky.neu.edu

1083-3668/2015/$25.00

were studying (i.e., the infrequency of arrival in the instrument FOV), (2) the large FOV (relative to cell size), and (3) the relatively large background autofluorescence and camera noise. We validated CV-IVFC, first in flow-phantom models with calibrated microspheres, and second in mice with injected multiple myeloma (MM) cells labeled with the vybrant-DiD near-infrared fluorescent dye. We demonstrated that CV-IVFC was capable of detecting and tracking circulating cells at concentrations of 20 cells/mL of circulating blood volume in a 30-min scan. This is potentially extremely valuable for applications involving rare circulating cells; for example, in measurement of the dissemination of circulating tumor cells in animal models of cancer metastasis where typical cell concentrations are on the order of 1–100 cells/mL. Moreover, unlike microscopy IVFC, CV-IVFC allows visualization of *in vivo* cell behavior of interest such as homing and docking events in the vasculature.

While our previous work demonstrated proof of principle of the approach, the performance of CV-IVFC as a function of fluorescence contrast (cell to background) was poorly understood. In general, three methods for fluorescent labeling of circulating cells for IVFC have been reported in the literature:[42] (1) *"ex-vivo"* labeling with a membrane-staining fluorescent dye such as vybrant-DiD (as in our previous work), (2) labeling of a cell line with a constitutively expressed fluorescent protein such as GFP, YFP, or mCherry, and (3) anti-body targeting of fluorophores. However, in general, methods (2) and (3) are expected to yield lower contrast than (1) due to increased autofluorescence and reduced light penetration associated with visible excitation and emission wavelengths (inherent to the physics of light propagation in biological tissue), or less efficient fluorescent probe targeting and uptake. Our initial "proof-of-principle" work used method (1), which represented a relatively high-contrast imaging model. Therefore, the performance of CV-IVFC with alternate fluorophores with lower contrast imaging conditions, such as (2) and (3) above, was of significant interest.

To address this issue, in the present work, we tested CV-IVFC with a series of tissue-mimicking optical phantoms with varying levels of autofluorescence, and with calibrated cell-simulating microspheres with varying fluorescent brightness. Depending on instrument parameters, CV-IVFC allowed robust detection of microspheres with significantly lower contrast; for example, detecting at least 50% of microspheres with over two orders of magnitude lower "heterogeneous contrast" (which we define as the number of high-intensity background pixels) than our previously reported *in vivo* conditions. Occurrence of false-positive detection events was found to correlate with temporal and spatial clustering of high-background pixels. As we discuss, these results are significant since they support the potential utility of CV-IVFC for a much wider range of biological models than our previous proof-of-principle studies.

2 Methods and Materials

2.1 *Computer Vision In Vivo Flow Cytometry Instrument*

A schematic diagram and photograph of the CV-IVFC instrument (as previously described in detail in Ref. 40), are shown in Figs. 1(a) and 1(b), respectively. The samples (mice or phantoms) were placed on the translation stage [Fig. 1(c)] and trans-illuminated with a 660 nm diode laser (DPSS-660; Crystalaser Inc., Reno, Nevada) filtered with a 660 nm "clean-up" filter (d660/20× Chroma Technology, Rockingham, Vermont) to remove any residual out-of-band light. A plano-convex lens pair (f = 50 mm and 200 mm; Edmund Optics, Barrington, New Jersey) expanded the beam to 5 mm at full width at half maximum at the sample where the laser intensity was 10 mW/cm^2. Light was collected with a 2× objective (2× Mitutoyo Plan Apo Infinity-Corrected Long WD Objective Edmund Optics, Barrington, New Jersey) and 1× lens tube. Fluorescence video sequences were obtained by placing a 710 nm filter (et710/50 m; Chroma) in the collection path. Video sequences were captured with a high sensitivity, 14-bit EMCCD camera (iXon^{EM} + 855 Andor Technology, Belfast, Northern Ireland) operating at a frame rate of 19 Hz. In combination with the collection lenses, this resulted in a ~5 × 5 mm^2 image. The EMCCD camera was also equipped with an adjustable gain setting, which was used in fluorescence image sequences. Monochrome white light images were also obtained by backillumination with a white-light source (Digi-Slave L-Ring 3200, Edmund Optics, Barrington, New Jersey) and removal of the 710 nm emission filter.

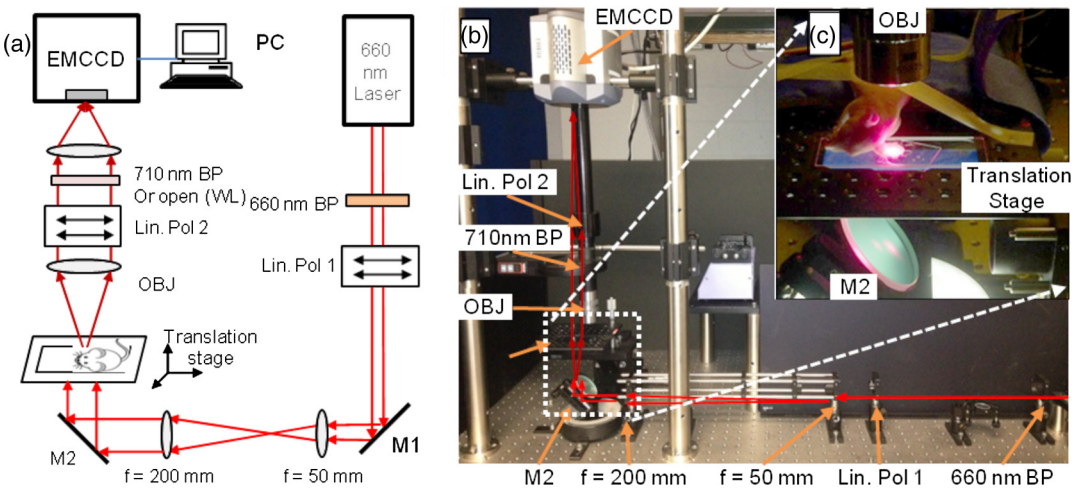

Fig. 1 (a) Schematic and (b) photograph of the computer vision *in vivo* flow cytometry (CV-IVFC) imaging system. M, mirror; Lin Pol; linear polarizer; Obj, 2x objective. (c) Photograph of a mouse ear positioned on the CV-IVFC imaging stage during data acquisition.

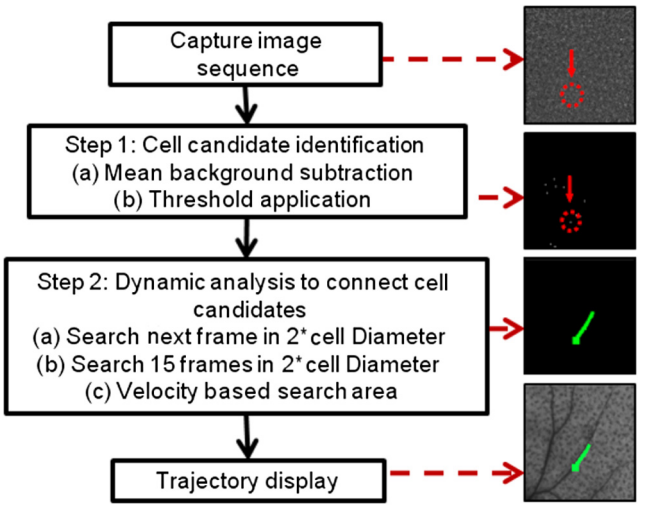

Fig. 2 Block diagram of the CV-IVFC tracking algorithm, showing major steps in the analysis. Cell candidates are identified (Step 1), and dynamically merged into trajectories (Step 2). The resulting cell trajectories are counted and overlaid on the white light image (see text for details).

2.2 *Computer Vision In Vivo Flow Cytometry Detection and Tracking Algorithm*

Given the large illumination area, circulating cells appeared as small targets (approximately 1 to 5 pixels in size) in image sequences. The relatively large tissue autofluorescence (see Sec. 3.1 below) and camera noise (due to gain) required discrimination of moving cells from the significant background signal. Moreover, the rarity of target circulating cell populations (< 1000 cells/mL) meant that their arrival in the imaging FOV was infrequent (about 1/min), making manual counting by a human operator tedious and error prone. To address this, we developed a computer vision algorithm to automatically detect and track circulating cells from image sequences. The details of this algorithm were previously described in detail in Ref. 40, but are restated here briefly for completeness: The algorithm (Fig. 2) was coded in MATLAB® (Mathworks, Natick, Massachusetts) and used two main analysis steps corresponding to "detect" and "connect" operations, respectively. In Step 1, cell candidates were identified by simple pixel-by-pixel mean background subtraction and comparison to a threshold. Any pixel or groups of pixels that exceeded this threshold were assigned "1" values (zero otherwise) and were classified as cell candidates. We ranked all pixel values and chose a threshold in the range from 99.90th to 99.99th percentile of maximum, which was previously determined to work well with *in vivo* data. In Step 2, the dynamic behavior of cell candidates was analyzed to "connect" them into cell trajectories. This step had multiple operations. First, when a cell candidate was identified, a search was performed inside a fixed radius from the candidate in the subsequent image in the sequence. Second, search regions ("cones") corresponding to the extrapolated position of the cell candidate given its last known position, speed, and direction were searched in the subsequent 15 images in the sequence. After completion of Step 2, any residual cell candidates that were not merged into trajectories were discarded, and all remaining trajectories were saved and counted by the algorithm as circulating cells. On a 64-bit personal computer with 16 GB of RAM, analysis of a 1000 frame video took approximately 2.5 min. The performance of the algorithm was analyzed for sensitivity and false alarm rate (See Sec. 2.4.2 below).

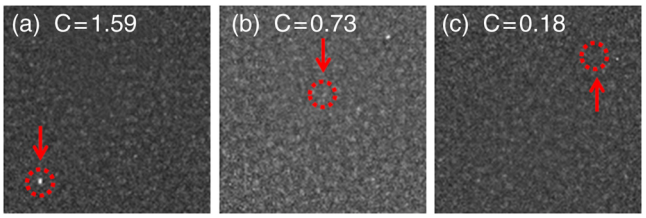

Fig. 3 Example images of circulating cells obtained from our previous *in vivo* studies[40] in which fluorescently labeled multiple myeloma (MM) cells were detected and tracked with CV-IVFC, along with the corresponding cell contrast for (a) high, (b) medium, and (c) low levels of contrast. The red circles and arrows indicate the position of the cell.

2.3 *Phantom Experiments*

We developed a set of tissue (ear) mimicking optical phantoms and used a series of cell-simulating fluorescent microspheres. Our goal was to produce imaging conditions with equal or lower contrast than our previous *in vivo* work. Example images from these studies where vybrant-DiD labeled MM cells were tracked in mice ears *in vivo* are shown in Fig. 3.[40] The variation in contrast (defined as $C = [I(s) - I(b)]/[I(b)]$, where $I(s)$ is the microsphere intensity and $I(b)$ is the mean background intensity in an image) is evident, and ranged between 0.18 and 1.59 (average of 0.73) between experiments, which we attribute primarily to differences in cell labeling. As we quantify in detail, the phantom experiments performed here yielded conditions with significantly lower contrast, allowing us to study the performance of the CV-IVFC with increased background autofluorescence or weaker cell labeling.

2.3.1 *Optical phantom preparation*

Tissue-mimicking optical phantoms were prepared by mixing polyester resin (Castin' Craft, Environmental Technology Inc., Fields Landing, California), TiO_2 powder (Sigma Aldrich, St. Louis, Missouri), and India Ink (Higgins, Leeds, Massachusetts) to approximately match the reduced scattering coefficient ($\mu_s' = 15$ cm^{-1}) and absorption coefficient ($\mu_a = 0.1$ cm^{-1}) of tissue at 700 nm.[43] To replicate the approximate dimensions of the mouse ear [Figs. 4(a) and 4(b)], the resin was placed in a 20-mm diameter and a 2-mm thick mold before hardening. The phantom material alone exhibited modest autofluorescence, so we added AlexaFluor (AF)-680 dye (Life Technologies, Carlsbad, California) to simulate biological tissue autofluorescence. Likewise, sebaceous glands are a prominent feature of *in vivo* fluorescence images in the mouse ear and appear as bright spots [Fig. 4(c)] that are occasionally falsely identified as circulating cells by the CV-IVFC algorithm. To mimic this, we added 6-μm fluorescent microspheres (Peakflow Claret cytometry beads, P-24670, Life Technologies) to the phantoms. In total, three sets of phantoms ($N = 3$ for each) were fabricated with either (1) P1; 0.4 μM AF680 and 850 microspheres per mL of resin material added, (2) P2; 0.4 μM AF680 and 1700 microspheres/mL added, or (3) P3; 0.6 μM AF680 and 1700 microspheres/mL added. Phantom type P2 corresponded to the approximate *in vivo* imaging conditions observed in our previous work, and type P3 represented a significantly elevated background fluorescence. Before hardening, a strand of Tygon tubing with a 250-μm internal diameter (TGY-010C, Small Parts, Inc., Seattle, Washington) was placed in the resin to simulate a blood vessel.

Example white light images of a phantom are shown in Figs. 4(d) and 4(e). Two example fluorescence images are also

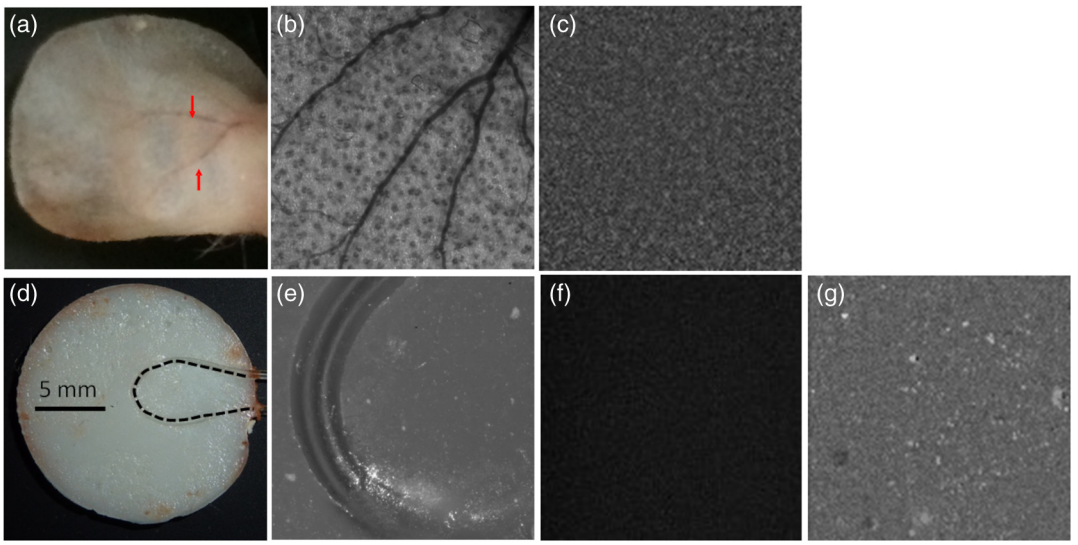

Fig. 4 Example images of a mouse ear (a-c) and optical phantoms (d-g). (a) Photograph of mouse ear with red arrows indicating large blood vessels. (b) White light image of the mouse ear taken with the CV-IVFC camera, (c) example fluorescence image of the same ear region with sebaceous glands and electron multiplied charge charge-coupled device (EMCCD) shot noise appearing as groups of bright pixels. (d) Photograph of a phantom with a dashed black line indicating the position of the embedded Tygon tubing. (e) White light image of the phantom taken with the EMCCD camera showing position of the Tygon tubing. (f) Fluorescence image of a phantom without fluorescent dye or microspheres added. (g) Fluorescence image of an example P2 phantom type, showing qualitative similarity to (c).

shown from a phantom without fluorescent material added, and with fluorescent material added (phantom type P2) in Figs. 4(f) and 4(g), respectively, showing the qualitative similarity to the *in vivo* fluorescence image shown in Fig. 4(c).

2.3.2 *Fluorescent microspheres*

We used calibrated fluorescent microspheres suspended in phosphate buffered saline to simulate circulating cells and flowed them through the phantoms using a microsyringe pump (70-2209, Harvard Apparatus, Holliston, Massachusetts) configured to produce a flow speed of 1.7 mm/s in the phantom tube (typical of flow speeds observed *in vivo*). To simulate the effect of different cell labeling techniques, we used a set of near-infrared microspheres with varying fluorescence intensities and with similar excitation and emission spectra to, e.g., Cyanine 5.5, Alexafluor-680. These are denoted as follows for the balance of this paper: MS1 (Peakflow Claret cytometry beads, Life Technologies), MS2 (Flash Red Intensity Standard FR5, Bangs Laboratories, Inc., Fishers, Indiana) and MS3 (Flash Red Intensity Standard FR4, Bangs). As shown in Fig. 5, these three microsphere types had fluorescence intensities equal to 200%, 62.8%, and 6.8% of the vybrant-DiD labeled MM cells that we used in our previous work. Therefore, this combination of spheres allowed us to test the performance of CV-IVFC with almost two orders of magnitude variation in fluorescence labeling.

2.4 *Computer Vision In Vivo Flow Cytometry Instrument Testing*

2.4.1 *Data acquisition*

We tested each of our three different phantom types with each of the three different fluorescent microspheres for a total of nine different contrast conditions. For each, microspheres suspensions of 2000 spheres/mL were used. The EMCCD camera exposure time was 0.05 s and the gain was set in the range of 10–30 (out of camera maximum 300) to fill the dynamic range of the camera. We collected approximately 5 min of video with a minimum of 25 spheres viewed for each phantom type.

2.4.2 *Performance metrics*

Video sequences were analyzed with the CV-IVFC algorithm and cell numbers and trajectories were recorded. Performance metrics for the algorithm were then calculated as follows:

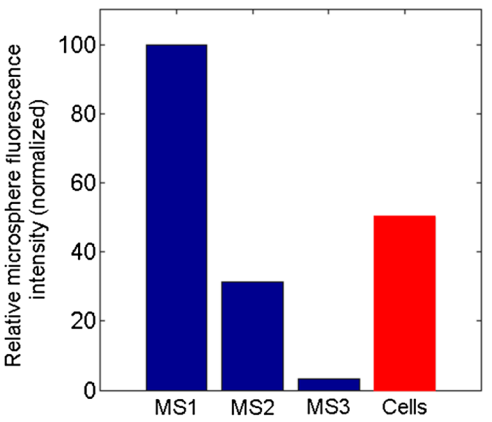

Fig. 5 Comparison of average fluorescence intensities of the three microsphere types (MS1, MS2, and MS3) used in these studies and vybrant-DiD labeled MM used in our previous work, normalized to MS1 intensity.

(1) sensitivity = TP/(TP + FN) where TP was the true positive count matching the ground truth and FN was the false-negative counts (i.e., cells missed by the algorithm), (2) false alarm rate (FAR), which was simply the number of false-positive counts per minute. The ground truth was taken as the result of a manual count by a human operator on the same image sequence. The metrics were computed for a range of threshold percentages from 99.90 to 99.99 of the maximum pixel from Step 1 in the algorithm.

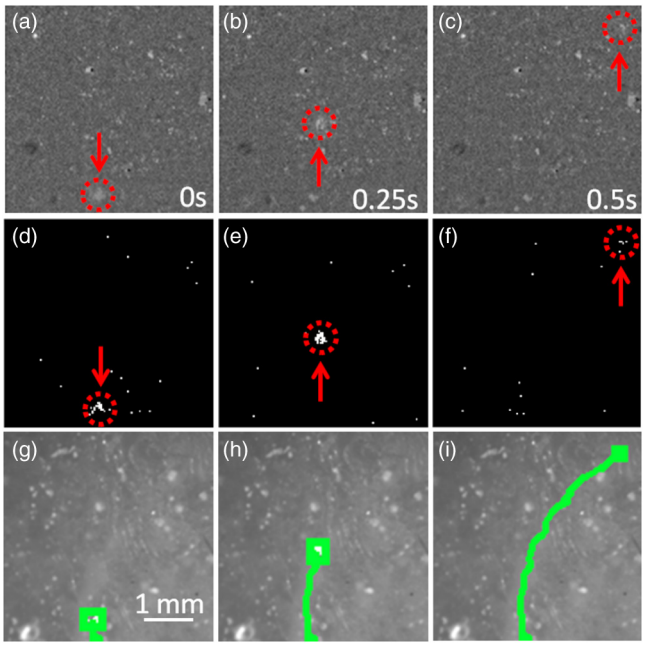

Fig. 6 Example image sequence of a single microsphere traveling through a phantom, separated by 0.25 s. Fluorescence (a-c) and (d-f) binary images obtained after the thresholding operation (Step 1) of the alogrithm are shown. Red circles and arrows indicate the position of the microsphere. In Step 2, dynamic analysis of image sequences was performed, and cell candidates were merged into trajectories, rejecting the stationary or spurious noise evident in (d-f). The recovered microsphere trajectory was overlaid (g-i) on the original white light image.

3 Results

3.1 *Computer Vision In Vivo Flow Cytometry Performance with Varying Background Intensity*

Example data generated by the CV-IVFC instrument are shown in Fig. 6. Here, an example fluorescence image sequence for phantom type P2 and MS1 is shown [Figs. 6(a)–6(c)] where each image frame is separated by 0.25 s. After microsphere candidates were identified in Step 1 [Figs. 6(d)–6(f)], they were merged into trajectories in Step 2 and then overlaid on white-light images [Figs. 6(g)–6(i)]. As shown, even though contrast was poor and significant background autofluorescence (AF680 and embedded fluorescent microspheres) was present in the phantom, the algorithm was capable of robustly distinguishing moving spheres from stationary background.

We systematically tested the CV-IVFC algorithm with phantoms with varying levels of background autofluorescence (phantom types P1-P3) with a single microsphere intensity (MS2). We analyzed image sequences and applied multiple detection thresholds in Step 1 of the algorithm as described in Sec. 2.2 above and in more detail in Ref. 40. Example representative results from three individual phantoms are summarized in Fig. 7. As indicated (and consistent with our previous work), the use of a lower threshold increased overall detection sensitivity [Fig. 7(a)] at the cost of increased FAR [Fig. 7(b)], whereas the use of a higher threshold reduced both parameters. In general, adjustment of this threshold allowed us to trade-off sensitivity and FAR with the system. Figures 8(a)–8(c) are three examples showing extracted microsphere trajectories overlaid on white light images, and (d) is an *in vivo* video sequence for comparison.

3.2 *Computer Vision In Vivo Flow Cytometry Instrument Performance with Varying Microsphere Intensity*

Next, we tested a single phantom (P2) with three different microsphere types with decreasing fluorescence intensities (MS1-MS3). Again, we computed sensitivity and FAR for a series of threshold values, and the data are summarized in Fig. 9. Generally, this followed the same trend as above, in that increasing the detection threshold resulted in lower sensitivity

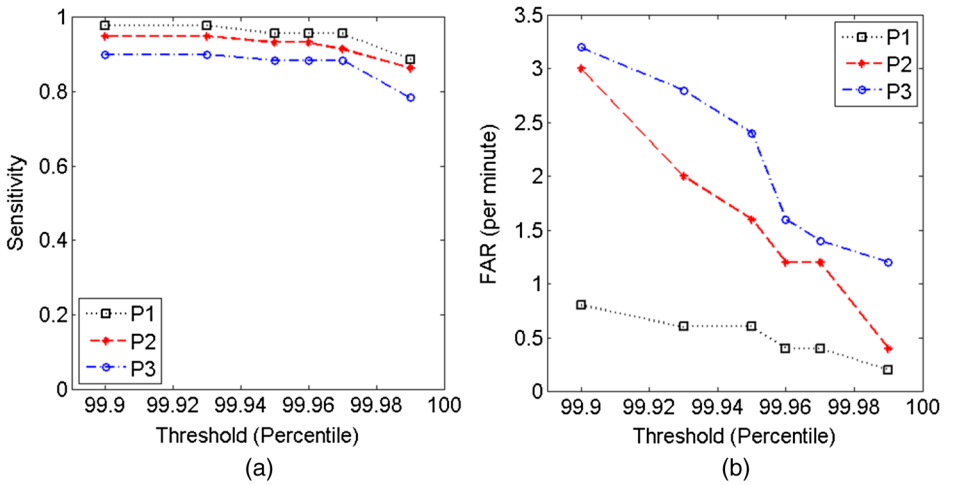

Fig. 7 (a) Sensitivity and (b) false alarm rate (FAR) as a function of threshold level (Step 1) for three different phantom types (P1, P2, and P3) and MS2 microspheres.

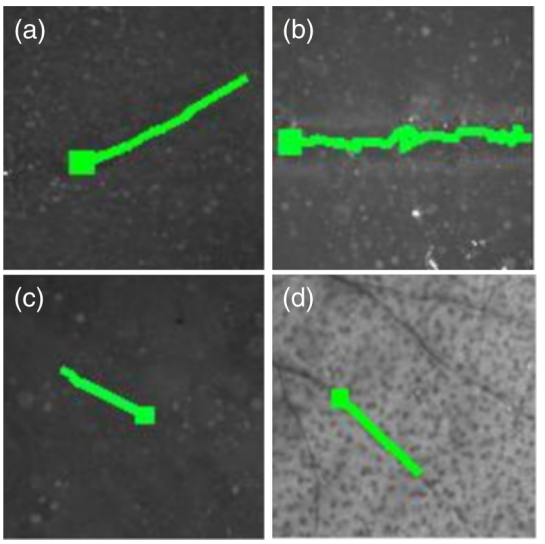

Fig. 8 Extracted microsphere trajectories overlaid on white light images for (a) phantom type P1 [Video 1 (http://dx.doi.org/10.1117/1.JBO.20.3.035005.1)], (b) phantom type P2 [Video 2 (http://dx.doi.org/10.1117/1.JBO.20.3.035005.2)], (c) phantom type P3 [Video 3 (http://dx.doi.org/10.1117/1.JBO.20.3.035005.3)], and (d) in a mouse ear *in vivo* [Video 4 (http://dx.doi.org/10.1117/1.JBO.20.3.035005.4)]. The left side of the video displays the original fluorescence image sequence, and the right side displays processed video (Video 1, QuickTime, 90 KB; Video 2, QuickTime, 707 KB; Video 3, QuickTime, 71 KB; Video 4, QuickTime, 72 KB).

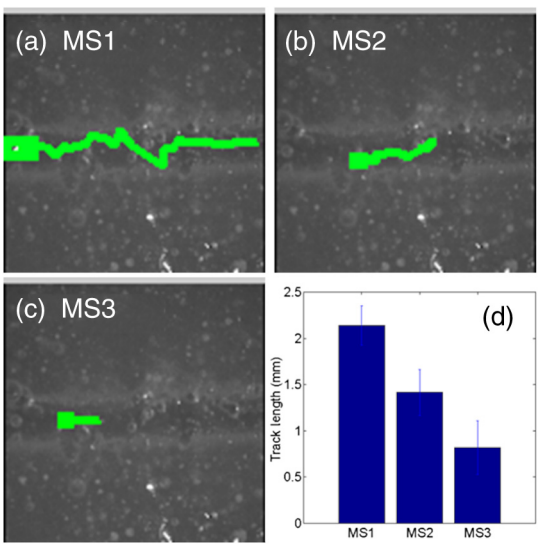

Fig. 10 Example microsphere trajectories obtained in phantom models for (a) MS1, (b) MS2, and (c) MS3 microsphere types for a single phantom type P2. (d) The average trajectory length for each of the microsphere types.

[Fig. 9(a)] and lower FAR [Fig. 9(b)]. We also note that, in general, shorter trajectories were extracted by the CV-IVFC algorithm in lower contrast conditions. Specifically, the average microsphere track lengths were 2.14, 1.42, and 0.82 mm for MS1, MS2, and MS3 types, respectively (see Fig. 10). Although circulating microspheres were visible for only brief periods in low contrast conditions, CV-IVFC was capable of robustly detecting them.

3.3 *Computer Vision In Vivo Flow Cytometry Instrument Performance Summary: All Conditions*

The overall performance of the CV-IVFC algorithm for the phantom and microsphere tests performed here is summarized in Fig. 11. We first considered the overall sensitivity of the algorithm for all 27 combinations (3 microsphere intensities × 9 phantoms) as a function of the image contrast. These data are shown in Fig. 11(a). (Here, we selected a threshold of the 99.95th percentile for the algorithm in Step 2, although this curve could be re-generated for any other threshold). All phantoms and microsphere combinations that we tested are shown, where the triangle markers correspond to MS1, squares to MS2, and circles to MS3. As indicated, although three sets of nominally identical phantoms were fabricated (P1–P3), significant inter-phantom variability was observed. For this reason, we plotted all individual data points (rather than means and standard deviations). As shown, the range of average contrasts (C) for different phantom-microsphere combinations was between 0.23 and 1.54, although the contrast of individual microspheres was as low as 0.06. For comparison, the range obtained from our earlier *in vivo* experiments is indicated in red [Fig. 3 and Ref. 40], where an average contrast of 0.73 was observed. By

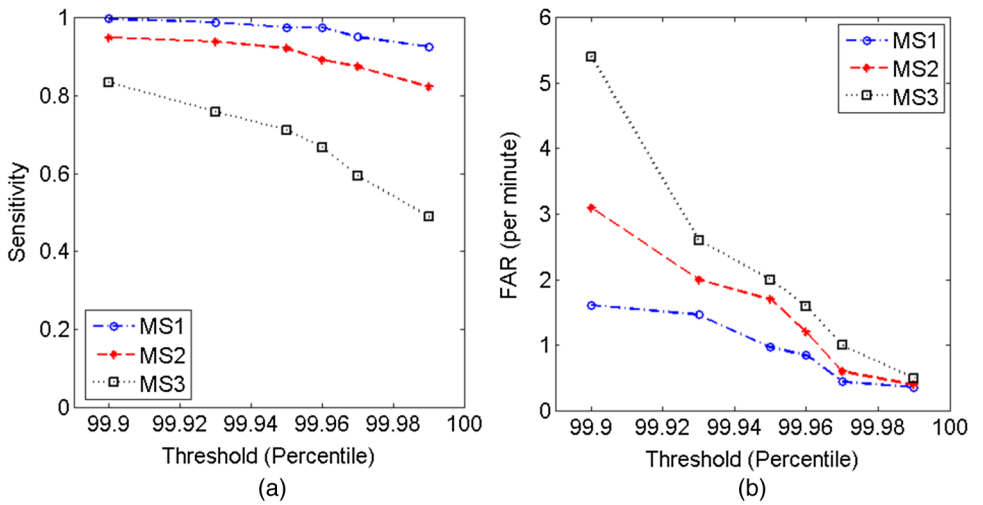

Fig. 9 (a) Sensitivity and (b) FAR as a function of threshold level (Step 1) for three different microsphere types (MS1, MS2, and MS3) and a P2 phantom type.

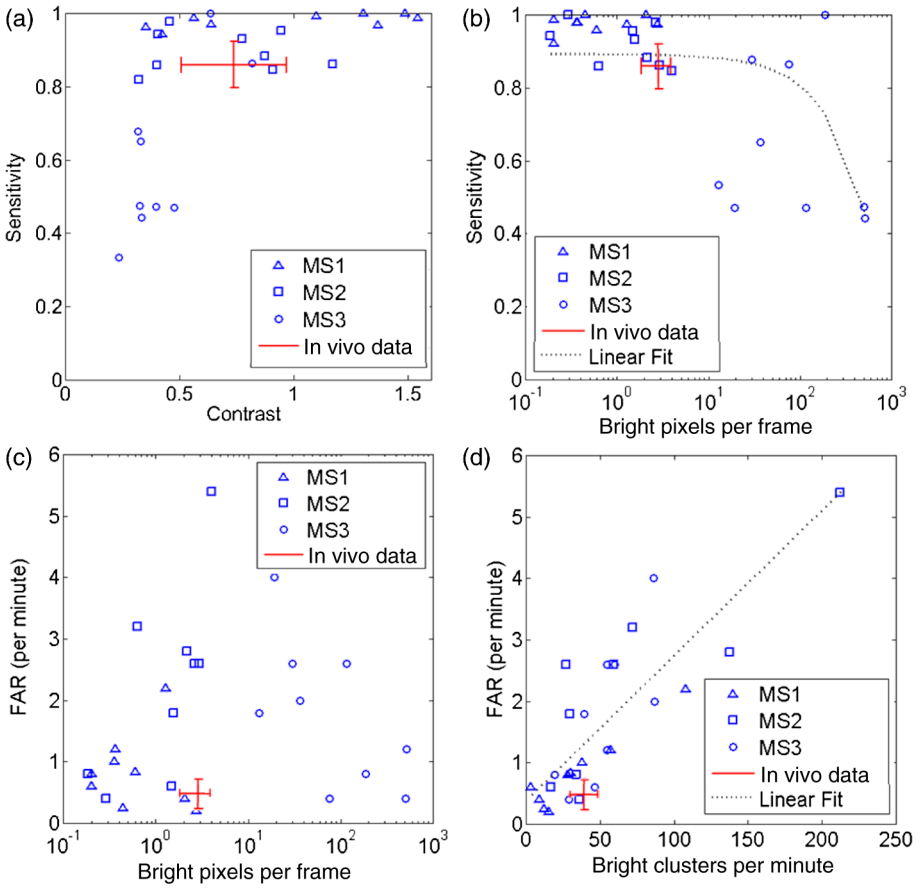

Fig. 11 (a) Sensitivity as a function of contrast for all phantoms and micosphere combinations tested. The mean and standard deviation sensitivity and bright pixel numbers for our previously acquired *in vivo* data are also plotted for comparison (red line). (b) Sensitivity as a function of "bright pixels" per frame (see text for definition) for experimental combinations tested. Unlike sensitivity, (c) FAR correlated poorly with "bright pixels" but correlated well with (d) "bright pixel clusters" per minute (see text for definition). Previous *in vivo* data are also shown for comparison in red. Dotted lines in (b) and (d) are linear fits to the data.

inspection, C was a poor predictor of algorithm performance for low contrast phantom-microsphere combinations (i.e., when $C < 0.5$), which as we have noted was our primary interest in this study. Review of our data suggested that the algorithm yielded highest tracking sensitivity when the background autofluorescence was relatively homogenous and could be effectively removed by subtraction. Therefore, as an alternative metric, we next considered the heterogeneity of the background intensity, which we defined as the number of "bright pixels" per frame in the image sequence [Fig. 11(b)]. Here, "bright pixels" were defined as the number of pixels per image after background subtraction that exceeded the mean intensity of a microsphere. In other words, these are the number of pixels where the noise on the pixel was comparable to the intensity of a microsphere. For the phantom experiments, a range of 0.2 to 518.3 bright pixels per image were observed, whereas on average 2.86 bright pixels per image was observed in our previous *in vivo* data. By inspection, the *in vivo* data generally agree with the phantom data, suggesting that our phantom-microsphere model mimicked *in vivo* imaging conditions well. Somewhat surprisingly [as shown in Fig. 11(c)], the number of bright pixels correlated only weakly with the FAR, since the CV-IVFC algorithm (Step 2) was efficient at rejecting bright pixels that were physically well separated. Further analysis revealed that a more complex quantity—the number of "bright pixel clusters" per minute—correlated well with FAR as shown in Fig. 11(d). Here, "bright pixel clusters" were defined as the number of occurrences for which two bright pixels were detected in subsequent image frames within a fixed radius (6 pixels). Analysis of our data indicated that, in general, these led to erroneous formation of microsphere trajectories. As above, our previous *in vivo* data were coplotted with the phantom data showing good general agreement. The implications of these results are discussed below.

4 Discussion and Conclusion

We recently developed and validated CV-IVFC as a new technology for detection, enumeration, and tracking of rare circulating cells in small animals *in vivo*. The major advantage of CV-IVFC compared to previous IVFC designs is the relatively large circulating blood volume that is sampled, leading to improved detection of low-abundance cells. We previously showed that this instrument was capable of detecting circulating cells in the range of 20 cells/mL. The purpose of the studies performed here was to characterize CV-IVFC under conditions of low imaging contrast compared to our previous *in vivo* studies.

The data in Fig. 11 summarize the effects of reduction in contrast from either mechanism. In combination, Figs. 11(a)

and 11(b) show the effect of loss of contrast (homogenous and heterogeneous) on detection sensitivity, and illustrate that CV-IVFC can effectively detect and track fluorescent targets with significantly lower contrast than in our previous *in vivo* studies. To quantify this, we considered the heterogeneous contrast data shown in Fig. 11(b). Although the parent function for these data is unknown, for comparison purposes we fit a linear function [dotted line on Fig. 11(b); note that this appears as a curve due to the logarithmic x-axis]. This fit implies that CV-IVFC would retain 80% detection sensitivity for the case corresponding to 109 bright pixels per image, which is equivalent to 38 times lower contrast versus our *in vivo* studies, where 2.86 bright pixels per image were observed on average. Likewise, 50% of microspheres would still be detected for the case of 457 bright pixels per image, corresponding to 159 times lower contrast. In practice, this reduction in contrast could come from either less-efficient fluorophore cell labeling, lower fluorescence quantum yield, or increase in background autofluorescence. This greatly increases the potential utility of CV-IVFC since it can be used with a wide range of fluorophores and labeling techniques. Absolute quantification of the mean equivalent soluble fluorochrome units for the microspheres was not available from the manufacturer, but comparison with our previous work and the literature values suggests that the intensity of the MS2 type would be comparable to a "typical" well-labeled cell. For example, comparison of extinction coefficient and emission quantum yield data suggests that cells labeled with the Turbo-FP650 red fluorescent protein (RFP; Evrogen, Moscow, Russia)[44–46] would be about three times less-brightly labeled than with vybrant-DiD. Likewise, the use of a green fluorophore would reduce the contrast by approximately a factor of 10 due to increased autofluorescence,[47–50] which (according to the analysis here) would not significantly degrade CV-IVFC sensitivity.

As we have noted, the relationship between FAR and bright pixels was more complex, since FAR was found to correlate with the number of "cell clusters" relating to both the temporal and spatial distribution of bright targets. In practice, this suggests that relatively high background autofluorescence can be tolerated by the algorithm without significant increase in FAR provided that bright pixels are physically separated in the image. As noted above, sensitivity and FAR can be traded-off by adjusting the "threshold" parameter in Step 1. In CV-IVFC, false alarms can be easily discounted by a human operator reviewing the original image sequence. Because the algorithm reports the time of detection in the image sequence, this is significantly more time efficient than manually counting cells with long (30 min or more) data acquisitions. Therefore, in practice, higher FAR is generally preferable to lower sensitivity in CV-IVFC.

We also note that the results shown here pertain specifically to our existing CV-IVFC instrument and algorithms and do not represent a technical limit of the technique. Improvement of the CV-IVFC tracking algorithm is the subject of ongoing work in our lab; we are currently pursuing a number of alternative strategies, for example, by jointly solving the "detect and connect" problem, as opposed to our current two-step process. Likewise, we have noted that stationary but distributed bright regions (such as sebaceous glands) appearing in multiple images frequently trigger false positives in the algorithm. As such, we are studying methods to automatically detect such regions and reject them as cell candidates. Therefore, we expect that a better CV-IVFC performance may be achieved in the future.

Acknowledgments

This research was supported by the National Institutes of Health, (R21HL098750; NHLBI), (R01EB012117; NIBIB), and Massachusetts Life Sciences Center. The authors acknowledge the valuable contributions of Dr. Binlong Li, Professor Octavia Camps, and Professor Mario Sznaier in development of CV-IVFC in our previous work.

References

1. M. Cristofanilli et al., "Circulating tumor cells, disease progression, and survival in metastatic breast cancer," *N. Engl. J. Med.* **351**, 781–791 (2004).
2. S. J. Cohen et al., "Relationship of circulating tumor cells to tumor response, progression-free survival, and overall survival in patients with metastatic colorectal cancer," *J. Clin. Oncol.* **26**, 3213–3221 (2008).
3. J. S. De Bono et al., "Circulating tumor cells predict survival benefit from treatment in metastatic castration-resistant prostate cancer," *Clin. Cancer. Res.* **14**, 6302–6309 (2008).
4. D. F. Hayes and J. B. Smerage, "Circulating tumor cells," *Prog. Mol. Biol. Transl. Sci.* **95**, 95–112 (2010).
5. M. Balic et al., "Circulating tumor cells: from bench to bedside," *Annu. Rev. Med.* **64**, 31–44 (2013).
6. J. W. Mellors et al., "Plasma viral load and CD4+ lymphocytes as prognostic markers of HIV-1 infection," *Ann. Intern. Med.* **126**, 946–954 (1997).
7. C. B. Coulam and R. G. Roussev, "Correlation of NK cell activation and inhibition markers with NK cytoxicity among women experiencing immunologic implantation failure after in vitro fertilization and embryo transfer," *J. Assist. Reprod. Genet.* **20**, 58–62 (2003).
8. S. Nagrath et al., "Isolation of rare circulating tumour cells in cancer patients by microchip technology," *Nature* **450**, 1235–1239 (2007).
9. S. Riethdorf et al., "Detection of circulating tumor cells in peripheral blood of patients with metastatic breast cancer: a validation study of the CellSearch system," *Clin. Cancer. Res.* **13**, 920–928 (2007).
10. H. W. Hou et al., "Isolation and retrieval of circulating tumor cells using centrifugal forces," *Sci. Rep.* **3**(1259) (2013).
11. H. M. Shapiro, *Practical Flow Cytometry*, 3rd ed., Wiley-Liss, New York (1995).
12. S. Barlage et al., *Cellular Diagnostics: Basic Principles, Methods and Clinical Applications of Flow Cytometry*, U. Sack, A. Tarnok, and G. Rothe, Eds., Karger Medical and Scientific Publishers, Basel, Switzerland (2008).
13. B. Weigelt, J. L. Peterse, and L. J. Van't Veer, "Breast cancer metastasis: markers and models," *Nat. Rev. Cancer* **5**, 591–602 (2005).
14. A. Ring, I. E. Smith, and M. Dowsett, "Circulating tumour cells in breast cancer," *Lancet Oncol.* **5**, 79–88 (2004).
15. B. Mostert et al., "Circulating tumor cells (CTCs): detection methods and their clinical relevance in breast cancer," *Cancer Treat. Rev.* **35**, 463–474 (2009).
16. M. Alunni-Fabbroni and M. T. Sandri, "Circulating tumour cells in clinical practice: methods of detection and possible characterization," *Methods* **50**, 289–297 (2010).
17. J. Novak et al., "In vivo flow cytometer for real-time detection and quantification of circulating cells," *Opt. Lett.* **29**, 77–79 (2004).
18. C. Alt et al., "Retinal flow cytometer," *Opt. Lett.* **32**, 3450–3452 (2007).
19. M. Hellerstein et al., "Directly measured kinetics of circulating T lymphocytes in normal and HIV-1-infected humans," *Nat. Med.* **5**, 83–89 (1999).
20. A. K. Azab et al., "CXCR4 inhibitor AMD3100 disrupts the interaction of multiple myeloma cells with the bone marrow microenvironment and enhances their sensitivity to therapy," *Blood* **113**, 4341–4351 (2009).
21. J. M. Runnels et al., "Optical techniques for tracking multiple myeloma engraftment, growth, and response to therapy," *J. Biomed. Opt.* **16**, 011006 (2011).
22. I. Georgakoudi et al., "In vivo flow cytometry: a new method for enumerating circulating cancer cells," *Cancer Res.* **64**, 5044–5047 (2004).
23. V. V. Tuchin, C. Greiner, and I. Georgakoudi, "Advances in fluorescence-based in vivo flow cytometry for cancer application," in

Advanced Optical Cytometry, Methods and Disease Diagnoses, V. V. Tuchin, Ed., pp. 463–500, Wiley-VCH Verlag GmbH & Co. KGaA, Weinheim, Germany (2011).
24. C. F. Zhong et al., "Quantitative two-photon flow cytometry: in vitro and in vivo," *J. Biomed. Opt.* **13**, 034008 (2008).
25. E. R. Tkaczyk and A. H. Tkaczyk, "Multiphoton flow cytometry strategies and applications," *Cytometry* **79**, 775–788 (2011).
26. V. P. Zharov, E. I. Galanzha, and E. V. Shashkov, "In vivo photoacoustic flow cytometry for monitoring of circulating single cancer cells and contrast agents," *Opt. Lett.* **31**, 3623–3625 (2006).
27. V. P. Zharov et al., "Photoacoustic flow cytometry: principle and application for real-time detection of circulating single nanoparticles, pathogens, and contrast dyes in vivo," *J. Biomed. Opt.* **12**, 051503 (2007).
28. V. P. Zharov, E. I. Galanzha, and V. V. Tuchin, "Photothermal image flow cytometry in vivo," *Opt. Lett.* **30**, 628–630 (2005).
29. V. V. Tuchin et al., "Towards in vivo flow cytometry," *J. Biophotonics* **2**, 457–458 (2009).
30. V. V. Tuchin, A. Tárnok, and V. P. Zharov, "In vivo flow cytometry: a horizon of opportunities," *Cytometry A* **79A**, 737–745 (2011).
31. E. I. Galanzha et al., "In vivo, non-invasive, label-free detection and eradication of circulating metastatic melanoma cells using two-color photoacoustic flow cytometry with a diode laser," *Cancer Res.* **69**, 7926–7934 (2009).
32. E. I. Galanzha and V. P. Zharov, "Photoacoustic flow cytometry," *Methods* **57**, 280–296 (2012).
33. E. I. Galanzha and V. P. Zharov, "Circulating tumor cell detection and capture by photoacoustic flow cytometry in vivo and ex vivo," *Cancers* **5**, 1691–1738 (2013).
34. Y. Li et al., "Circulation times of prostate cancer and hepatocellular carcinoma cells by in vivo flow cytometry," *Cytometry A* **79**, 848–854 (2011).
35. V. V. Tuchin, S. P. Morgan, and I. M. Stockford, *Instrumentation for In Vivo Flow Cytometry: Sickle Cell Anemia Case Study*, Wiley-VCH Verlag GmbH & Co. KGaA, Weinheim (2011).
36. Z. Fan et al., "In vivo tracking of 'color-coded' effector, natural and induced regulatory T cells in the allograft response," *Nat. Med.* **16**, 718–722 (2010).
37. E. Zettergren et al., "Instrument for fluorescence sensing of circulating cells with diffuse light in mice in vivo," *J. Biomed. Opt.* **17**, 037001 (2012).
38. E. Zettergren et al., "Tomographic sensing and localization of fluorescently labeled circulating cells in mice in vivo," *Phys. Med. Biol.* **57**, 4627–4641 (2012).
39. N. Pestana et al., "Improved diffuse fluorescence flow cytometer prototype for high sensitivity detection of rare circulating cells in vivo," *J. Biomed. Opt.* **18**, 077002 (2013).
40. S. Markovic et al., "A computer vision approach to rare cell in vivo fluorescence flow cytometry," *Cytometry Part A* **83**, 1113–1123 (2013).
41. V. Pera et al., "Maximum likelihood tomographic reconstruction of extremely sparse solutions in diffuse fluorescence flow cytometry," *Opt. Lett.* **38**, 2357–2359 (2013).
42. C. M. Pitsillides et al., "Cell labeling approaches for fluorescence-based in vivo flow cytometry," *Cytometry A* **79**, 758–765 (2011).
43. J. Baeten et al., "Development of fluorescent materials for diffuse fluorescence tomography standards and phantoms," *Opt. Express* **15**, 8681–94 (2007).
44. M. Z. Lin et al., "Autofluorescent proteins with excitation in the optical window for intravital imaging in mammals," *Chem. Biol.* **16**, (2009).
45. D. Shcherbo et al., "Near-infrared fluorescent proteins," *Nat. Med.* **7**(10), 827–829 (2010).
46. D. Shcherbo et al., "Bright far-red fluorescent protein for whole-body imaging," *Nat. Methods* **4**, 741–746 (2007).
47. R. M. Hoffman, "Advantages of multi-color fluorescent proteins for whole-body and in vivo cellular imaging," *J. Biomed. Opt.* **10**(4), 041202 (2005).
48. N. C. Deliolanis et al., "Performance of the red-shifted fluorescent proteins in deep-tissue molecular imaging applications," *J. Biomed. Opt.* **13**, 044008 (2008).
49. B. N. G. Giepmans et al., "The fluorescent toolbox for assessing protein location and function," *Science* **312**, 217–224 (2006).
50. E. J. Sutton et al., "Cell tracking with optical imaging," *Eur. Radiol.* **18**, 2021–2032 (2008).

Stacey Markovic is a PhD candidate at Northeastern University in Boston, Massachusetts. She received her BS degree in electrical engineering from Northeastern University in 2008 and her MS degree in biomedical engineering from Boston University in 2010. Her research includes optical enumerating and tracking of rare circulating cells *in vivo*.

Siyuan Li received his BS degree in electrical engineering at Northeastern University in Boston, Massachusetts, in 2014. His research includes computer vision algorithms and data processing.

Mark Niedre is an associate professor of electrical and computer engineering at Northeastern University. He received his PhD degree from the University of Toronto in the Department of Medical Physics in 2004.